Biosensors and Bioelectronics 141 (2019) 111479

Contents lists available at ScienceDirect

Biosensors and Bioelectronics

journal homepage: www.elsevier.com/locate/bios

Co_3O_4 needles on Au honeycomb as a non-invasive electrochemical biosensor for glucose in saliva

Victoria E. Coyle[a,b], Ahmad E. Kandjani[a], Matthew R. Field[c], Patrick Hartley[b], Miao Chen[a,b], Ylias M. Sabri[a,**], Suresh K. Bhargava[a,*]

[a] Centre for Advanced Materials and Industrial Chemistry (CAMIC), School of Science, RMIT University, Melbourne, Victoria, 3001, Australia
[b] CSIRO, Bayview Avenue, Clayton, Victoria, 3168, Australia
[c] RMIT Microscopy & Microanalysis Facility, RMIT University, Melbourne, Australia

ARTICLE INFO

Keywords:
Glucose biosensor
Electrochemical detection
Saliva
Non-invasive
Porous gold
Cobalt oxide

ABSTRACT

While glucose monitoring technology is widely available, the continued prevalence of diabetes around the world coupled with its debilitating effects continues to grow. The significant limitations which exist in the current technology, instils the need for materials capable of non-invasive glucose detection. In this study a unique non-enzymatic electrochemical glucose sensor was developed, utilising a gold honeycomb-like framework upon which sharp Co_3O_4 needles are anchored. This composite nanomaterial demonstrates excellent sensing performance in glucose concentrations ranging between 20 μM and 4 mM, exceeding the range required for non-invasive glucose sensing. In conjunction with this high sensitivity (2.014 mA $mM^{-1} \cdot cm^{-2}$), the material possesses excellent selectivity towards glucose for commonly interfering physiological species such as uric acid and ascorbic acid. Glucose detection in synthetic saliva was then performed showing excellent capability in the low concentration range (20 μM–1 mM) for non-invasive sensing performance. Further tests showed good selectivity of the sensor in physiological contaminants commonly found in saliva such as cortisol and dopamine. This development provides excellent scope to create next-generation non-invasive diabetes monitoring platforms, with excellent performance when detecting low glucose concentrations in complex solutions such as saliva.

1. Introduction

Diabetes continues to grow as a major global health challenge with 422 million adults currently afflicted with this disease, with indicators pointing to this figure doubling by the year 2030 (Barry et al., 2017). In the United States alone, the estimated cost of diabetes in 2017 was $327 billion (Association, 2018), highlighting the scale of the problem and the need for improved detection and treatment options. Whilst methods to monitor glucose concentrations are currently in widespread use, these detection methods are predominantly centred around blood-based detection which are non-user friendly as they involve frequent invasive and painful sampling procedures. Due to these pitfalls there is great demand for technology which will support non-invasive glucose detection for diabetes monitoring (Bandodkar and Wang, 2014). Alternative strategies to detect glucose include monitoring urine (0–0.8 mM glucose, enzymatic method) (Lankelma et al., 2012), saliva (0.03–0.08 mM glucose, non-enzymatic methods) (Raymundo-Pereira et al., 2016; Ye et al., 2013), sweat (0.02–0.6 mM glucose, non-enzymatic method) (Anderson et al., 2017; Moyer et al., 2012), tears (0.1–0.6 mM glucose, enzymatic methods) (Kownacka et al., 2018; Yao et al., 2011) or breath (0.4–4 mM glucose, enzymatic method) (Roberts et al., 2012) based samples. The glucose concentrations for these alternative modes of detection are much lower than concentrations in blood (4.4–6.6 mM glucose) (Wang, 2008) meaning effective sensors for these non-invasive modes of analysis require a high degree of sensitivity. Moreover, their applicability is underpinned by their stability as well as their ability to selectively detect glucose in the presence of physiological contaminants such as ascorbic acid (AA) and uric acid (UA). These contaminants tend to disrupt the performance of chemical sensing results (Cheng et al., 2010; Zhang et al., 2011) by capping the active sites of electrode surfaces. While enzymatic glucose sensors have been investigated, they pose many issues such as poor stability, low reproducibility and limitations due to the need for an oxygen source (Wang et al., 2013; Zhu et al., 2016). Non-enzymatic glucose sensors are therefore an attractive option to overcome these issues, allowing for increased selectivity through low onset potentials, higher sensitivities

* Corresponding author.
** Corresponding author.
E-mail addresses: ylias.sabri@rmit.edu.au (Y.M. Sabri), suresh.bhargava@rmit.edu.au (S.K. Bhargava).

https://doi.org/10.1016/j.bios.2019.111479
Received 24 December 2018; Received in revised form 28 May 2019; Accepted 24 June 2019
Available online 26 June 2019
0956-5663/

and improved stability due to the use of inorganic components in comparison to their biological counterparts (Toghill and Compton, 2010). Of the current non-enzymatic materials showing promise for glucose detection, Au has attracted much attention due to its high sensitivity but more specifically its excellent selectivity (Chakraborty et al., 2019). This excellent selectivity is attributed to its increased surface area-volume ratio, low applied onset potentials, control of structure fabrication for the nanostructures shape, size or porosity and active site density (Boisselier and Astruc, 2009; Coyle et al., 2016). Extending upon the properties of a mono-metallic structure, the addition of a metal oxide has also shown much success in non-enzymatic glucose sensing (Ding et al., 2010; Tong et al., 2012; Wang et al., 2009). Co_3O_4 in particular has excellent biocompatibility, high electrocatalytic activity and adsorption capacity for glucose making it very appealing to sensing fabrications (Kimmel et al., 2011; Solanki et al., 2011). Although Co_3O_4 shows great promise, its poor electronic conductivity limits its success to display high sensitivity, reliability and rapid response times (Ding et al., 2010; Solanki et al., 2011). A proposed method to combat these issues is to mould the Co_3O_4 to an Au scaffold structure allowing for the positive features of each material (Lang et al., 2013) to take prominence and reduce the effects of their pitfalls. The synergistic effect of the two present materials will allow for the lower sensitivities of Au and the poor selectivity of Co_3O_4 to no longer be an issue (Lay et al., 2017). In this work the fabrication of a composite nanostructure is investigated, bringing together Au and Co_3O_4. Through the adoption of a synthesis procedure which has been previously shown to create highly porous nanomaterials, a gold scaffold is synthesised which can then be modified with Co_3O_4 in a facile manner. The potential for the use of this unique nanomaterial in non-invasive glucose sensing is then investigated using a chronoamperometric protocol.

2. Experimental

All chemicals used in this work were purchased from Sigma-Aldrich and used as received. Au films were prepared using an e-beam evaporation method utilising an adhesion layer of 150 nm Ti, followed by a 150 nm layer of Au on a Si wafer. The Si/Ti/Au wafers were then diced into 8 mm × 18 mm substrates and masked with Kapton tape to reveal an exposed region of 0.238 cm^2 (diameter of 5.5 mm).

2.1. Synthesis of Au honeycomb

Electrochemistry experiments were performed using a CH instrument (CHI760C) workstation with an attached amp booster (model 680). The developed substrate, a graphite rod and Ag/AgCl 3 M KCl (+0.197 V vs SHE) probe were used as the working, counter and reference electrodes, respectively. Electrodeposition of the hydrogen bubble templated Au was performed at −4 V for 300 s, in a solution of 10 mM $HAuCl_4$ and 2 M H_2SO_4, in accordance with our previous studies (Scheme 1A and 1B) (Coyle et al., 2016; Plowman et al. 2010, 2011).

2.2. Synthesis of Au honeycomb/Co_3O_4 needles

Hydrothermal synthesis of cobalt hydroxide on the honeycomb-like gold surface was obtained by placing $CoCl_2{\cdot}6H_2O$ (5, 10, 25, 50 and 100 mM) and urea (60 mg) into a 6 mL capacity Teflon-lined stainless steel autoclave (Dong et al., 2012). The electrodeposited substrate was then placed into the solution standing with a 45° tilt facing the autoclave wall. The autoclave was then sealed and placed into an oven at 100 °C for 5 h. The plain Au and modified cobalt hydroxide samples were then washed with Milli-Q water, dried under N_2 gas and annealed in air at 450 °C for 2 h for the conversion of cobalt hydroxide to cobalt oxide (Scheme 1C and 1D).

2.3. Characterization

Scanning electron microscopy (SEM) was used to analyse the surface morphology by comparing the needle growth for each concentration of Co_3O_4. SEM was performed using an FEI Verios 460L equipped with an Oxford Instruments $XMax^N20$ energy dispersive x-ray spectroscopy (EDX) detector. SEM imaging was performed using an accelerating voltage of 10 kV and EDX was performed at 15 kV. To view the cross section of the structures, the samples were milled using a gallium ion beam (operating at 30 kV) in an FEI Scios Dualbeam FIB. X-ray diffraction (XRD) was performed using a Bruker D8 Discover micro diffraction system with a general area diffraction detector system. A Cu-Kα radiation source was used with an operating voltage of 40 kV with a current of 40 mA. X-ray photoelectron spectroscopy (XPS) was performed to determine the oxidation state of the Au, Co and O formed on the surface, using a Thermo K-alpha XPS, (Al Kα = 1486.7 eV). The core level binding energies (BEs) were aligned with the adventitious C 1s binding energy of 284.8 eV.

2.4. Electrochemical glucose sensing in alkaline media

Cyclic voltammetry (CV) was employed using a scan rate 20 mV s^{-1} in a solution of 0.5 M KOH and 10 mM glucose. Chronoamperometry was then used with a basic solution of 0.5 M KOH with glucose additions between 20 μM and 10 mM. Physiological contaminants were analysed using chronoamperometry with individual additions of 0.1 mM of sucrose, fructose, maltose and lactose and 0.02 mM of ascorbic acid and uric acid. Current density was calculated using the geometric surface area value of 0.238 cm^2 to enable comparison with sensors reported in literature.

2.5. Electrochemical glucose sensing in synthetic saliva

CV analysis was employed using a scan rate of 50 mV s^{-1} in a solution of synthetic saliva followed by the addition of 0.06 mM glucose. The synthetic saliva was prepared according to the AFNOR NF S91-141 standard which consists of Na_2HPO_4 (1 mM), KH_2PO_4 (1.5 mM), $NaHCO_3$ (18 mM), KSCN (3 mM), NaCl (115 mM) and KCl (16 mM) (Chaisiwamongkhol et al., 2017). Chronoamperometric additions analysis was then performed in synthetic saliva with increasing additions of glucose ranging between 0.02 mM and 1 mM. Physiological contaminants present in saliva were performed using continuous chronoamperometric additions analysis with individual additions of 2.4 μM ascorbic acid, 1.6 μM dopamine and uric acid (Raymundo-Pereira et al., 2016) followed by 0.22 μM of cortisol.

3. Results and discussion

3.1. Au honeycomb/Co_3O_4 needle characterization

The developed hydrogen bubble templated Au honeycombs are shown in Fig. 1A displaying a highly porous large structure which formed evenly across the surface of the substrate. Fig. 1B shows the formation of the pores atop the surface of the substrate whilst retaining exposed areas of bare substrate through the porous material. The fractal formations of the hydrogen bubble templated Au which show the consistent accumulation of small Au nanostructures (~100–200 nm) are displayed in Fig. 1C–D. Smooth branched formations of Au have grown upwards from the substrate allowing for multiple active sites across the material (Coyle et al., 2017). The pure hydrogen bubble templated Au was then coated with different concentrations of $CoCl_2$ (5, 10, 25, 50 and 100 mM) through the hydrothermal technique mentioned above (Supplementary information S1A-F). The 5 mM surface (Supplementary information S1B) showed minimal growth of needles over the Au structures, with increasing concentrations of $CoCl_2$ leading to an increase in both length and spread of formations. 10 mM $CoCl_2$

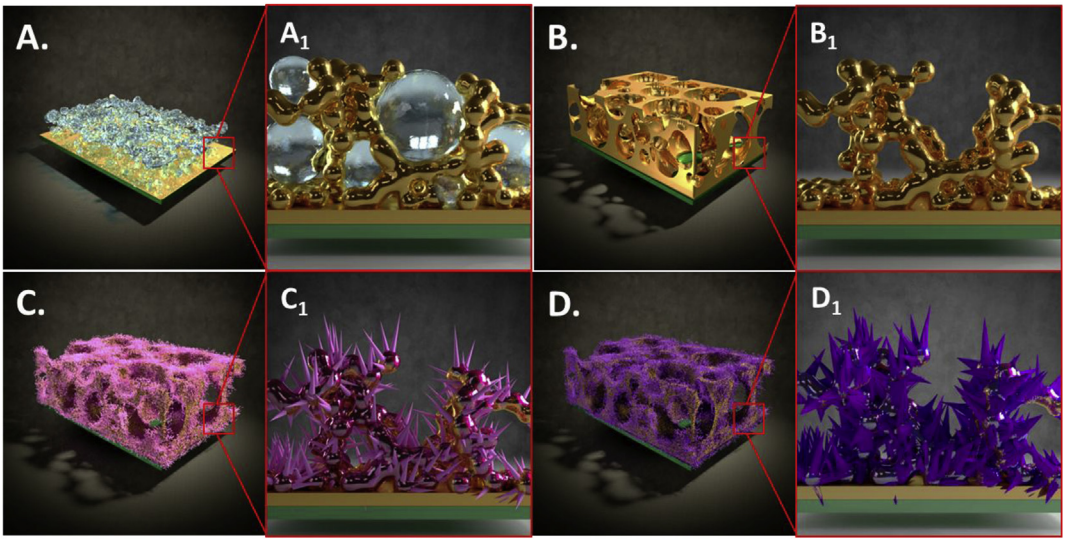

Scheme 1. Schematic (representing low (left) and high (right) magnifications) of Au lattice formation (A) and (B) with the growth of cobalt hydroxide (C) followed by the conversion to cobalt oxide (D).

(Supplementary information S1C) and upwards, caused the needle formations to become visible at the edges of the pores. Increasing the concentration to 25 mM (Supplementary information S1D) caused a coating of needles along the top side of the structure, with the needle lengths increasing in length as the concentration was increased to 50 mM (Supplementary information S1E). The 100 mM concentration (Supplementary information S1F) appears to have completely coated the Au scaffold with obvious needle lengths increasing dramatically compared to the lower concentrations of $CoCl_2$. Due to the coherent nature of the Co_3O_4 formation across the surface of the Au scaffold, all characterization and sensing studies were then focused on the 100 mM $CoCl_2$ sample. As is seen in Fig. 1E, the needle nanostructures have formed seamlessly across the Au scaffold whilst the pores remained unimpeded, which can be further seen in Fig. 1F. Long, sharp, needles are shown in Fig. 1G with Fig. 1H showing the needles are comprised of multiple nanoparticles forming the structure. Side imaging was performed after slicing of the material using a gallium ion beam (Fig. 2A) to see how the needles formed within the Au scaffold. Backscatter imaging was then performed (Fig. 2B) where the darker regions represent Cobalt formations and the lighter regions represent Au. Analysis of high magnification images (Fig. 2C and D) showed the growth of the needles spreading throughout the Au structure. This coating (the needle-like structures) atop the Au commenced their growth both within the Au scaffold and along the top of the surface. EDX mapping of the side imaging confirms the presence of both Au (Supplementary information S2A) and Co (Supplementary information S2B) throughout the entirety of the sample, as opposed to only coating the top surface of the Au structure. Reproducibility of the sensor surfaces was performed by repeating the synthesis of the 100 mM $CoCl_2$ 3 times (Supplementary information S3). From SEM images, repeated synthesis of the cobalt oxide rods across the surface is easily obtained via both needle length and spread across the Au scaffold. Comparison of the needle formations both pre and post annealing at 450 °C were analysed using SEM imaging (Supplementary information S4A and S4B). The pre-annealed needles are observed to have a very smooth surface, whereas the needles post-annealing formed stacked particles whilst maintaining a needle-like shape (Supplementary information S4C and S4D). EDX analysis of the 100 mM $CoCl_2$ samples, presented in Fig. 3A shows clear peaks for Au, Co and O showing they are the three prominent materials in the sample, with calculated abundancies of Au: 44.6 wt%, Co: 23.9 wt% and O: 12.2 wt%. The appearance of Si in the EDX analysis is attributed to the Si substrate (7.4 wt%). To clarify the formed type of Co_xO_y aggregate, XRD analysis (Fig. 3B) was performed to analyse the crystalline structure. Significant peaks in the XRD patterns appear at $2\theta = 38.4$, 44.2, 64.4, 77.9 and 81.7° which are attributed to (111), (200), (220), (311) and (222) planes of the FCC Au structure, respectively (JCPDS card no. 04-0784). Smaller and less defined peaks appear at $2\theta = 18.9$, 31.3, 56.3 and 59.4° which can be attributed to the (111), (220), (311), (422) and (511) planes of Co_3O_4, respectively (JCPDS card no. 01-071-0816). Other peaks attributed to Co_3O_4 have been hidden by the large amount of Au in the sample, with overlapping possible between the (222), (400) and (440) peaks of Co_3O_4 and the (220), (311) and (222) planes of Au. From the XRD analysis all non-Au peaks are attributed to the common Co_3O_4 spinel phase, describing good crystalline arrays (Ibupoto et al., 2014). Further confirmation of the oxidation states of the Au, Co and O were performed using XPS analysis. The survey spectra of the formed material is shown in Fig. 3C, displaying peaks for C, Au, O and Co. Deconvolution of elemental XPS spectra for the Au (Fig. 3D), Co (Fig. 3E) and O (Fig. 3F) was used to determine the elemental states of the materials present. The main peak at 84.0 eV is attributed to the Au $4f_{7/2}$ binding energy representing the Au^0 core level (Casaletto et al., 2006; Daima et al., 2013; Kabir et al., 2015; Pearson et al., 2011) with a corresponding doublet peak at 87.7 eV. The Co 2p spectra is consistent with previous studies comparing results obtained for different phases of cobalt species such as $Co(OH)_2$, CoO and Co metal (Biesinger et al., 2011). Two main peaks lying at 780.3 and 795.4 eV represent the Co $2p_{3/2}$ and Co $2p_{1/2}$ spin-orbital lines, respectively (Liu et al., 2014; Mei et al., 2012). Upon deconvolution of the Co $2p_{3/2}$ peak it becomes apparent that both Co(II) and Co(III) oxidation states are present which is consistent with Co_3O_4. The assurance of cobalt oxide (Co_3O_4) is further deduced from the presence of two satellite peaks (789.9 and 795.4 ev) with low intensity which have shifted to a higher binding energy, agreeing well with previous reports (Yang et al., 2010). The peak at 529.9 eV in the oxygen spectra is denoted as the O 1s peak (Nohira et al., 2002) with a satellite peak at 531.5 eV due to possible hydroxides remaining on the surface after annealing.

3.2. Au honeycomb/Co_3O_4 needle electrochemical sensing

To analyse the applicability and on-set potential of the synthesised Au/Co_3O_4 sensor for glucose sensing, cyclic voltammetry (CV) and chronoamperometry techniques were used. These techniques allowed for the analysis of both the surface affinity, thus rate of reaction towards glucose (e.g. sensitivity) and selectivity in the presence of common physiological contaminants. CV analysis was performed at a scan rate of 20 mV s^{-1} to examine the oxidation and reduction

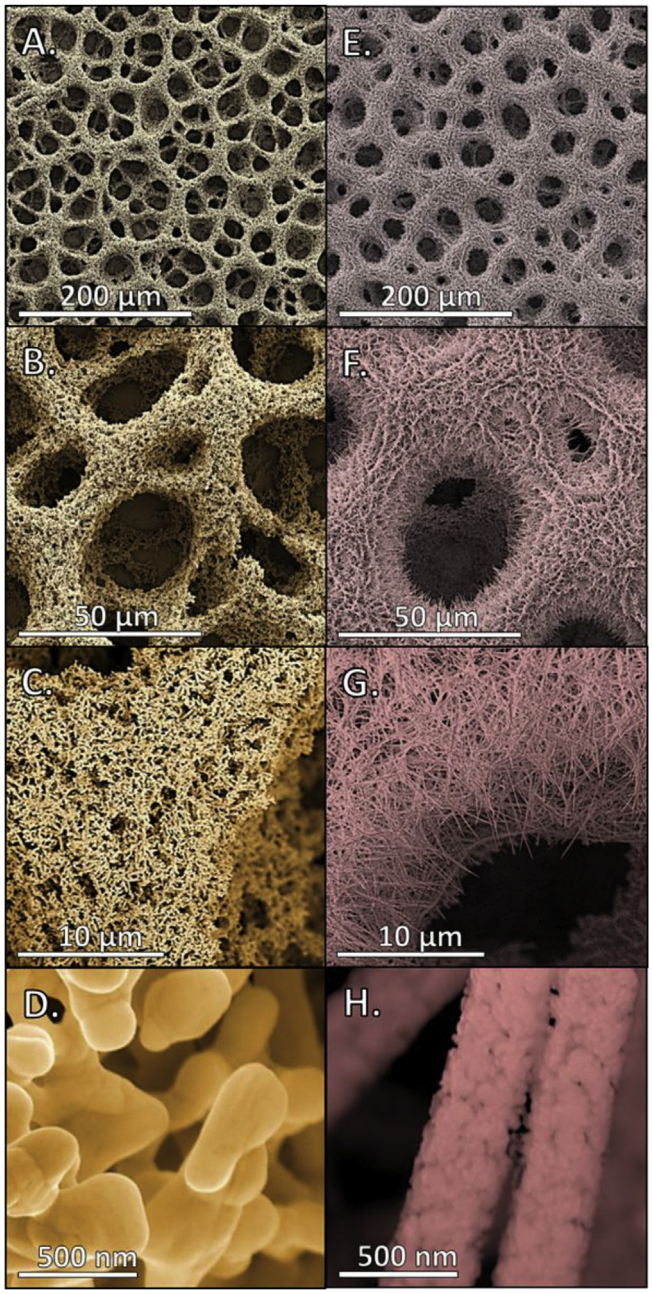

Fig. 1. SEM images (false colour) of Au honeycomb (left panel) and Au honeycomb coated with 100 mM $CoCl_2$ (right panel) at different magnifications (A and E) 200 µm, (B and F) 50 µm, (C and G) 10 µm and (D and H) 500 nm. (For interpretation of the references to colour in this figure legend, the reader is referred to the Web version of this article).

reactions the Au/Co_3O_4 undergoes in the presence of 10 mM glucose (Fig. 4A). For the continued studies 20 mV s^{-1} was chosen as the applied scan rate due to sweep rate analysis varying between 10 and 500 mV s^{-1} (Supplementary information S5) for optimal performance. From the sweep rate analysis, the increase in anodic peak height along with a shift in the peak potential as the scan rate increased was observed. The linearity of the peak increase indicates the redox process of a diffusion-controlled mechanism (Bertoncello and Ugo, 2003). This phenomenon proves the interaction between KOH, glucose and the Au/Co_3O_4 occurs at the electrode surface whilst maintaining electrode electroneutrality (Teixeira et al. 2004a, 2004b). From CV analysis at 20 mV s^{-1}, two large peaks were observed at +0.25 V in the forward scan and +0.1 V in the reverse scan. The large sharp peaks at each of these points along the CV curve display a combinatory electroactivity between the Au and Co_3O_4 species in the modified Au/Co_3O_4 surface (Lang et al., 2013). The broad oxidation peak at +0.25 V can be attributed to the formation of gluconolactone with the conversion of Co_3O_4 to CoO_2 due to the reactions of glucose + AuOH and glucose + Co_3O_4 (Ding et al., 2010). As the potential increased above +0.3 V the formation of Au_2O_3 caused a reduction of AuOH present on the surface impeding the oxidation of glucose (Han et al., 2014). In the reverse scan the reduction of Au_2O_3 formed large amounts of AuOH and formate (Aoun et al., 2004) which allowed for a large number of active sites to be regenerated on the electrode surface. This occurrence makes way for more glucose molecules to react with the surface thus producing excellent electroactivity. The Au/Co_3O_4 forms a much larger anodic current for the negative scan due to the diffusion effect by the junction of Au and Co_3O_4. As the oxide is stripped in the reverse scan, more glucose is present near the electrode surface which in turn produces a much larger enhancing the electrocatalytic activity of the sensor (Chen et al., 2010). The individual reactions are discussed below. The Au component of the surface undergoes electrosorption of glucose at low potentials which ignites the accumulation of contaminant intermediates on the electrode surface blocking the active surface sites. The formation of AuOH occurs as the potentials begin to increase which is due to the partial discharge of OH^- ions. This discharge of ions is able to catalyse glucose, forming the absorbed intermediate gluconolactone which then allows for the oxidation of Au to form AuO. This AuO formation can inhibit the electrooxidation of glucose however a further step occurs, which consists of Au being regenerated due to the AuO converting back to Au(OH) as the potentials are reduced (Ding et al., 2011). The overall reaction is described in Eqn. (1) (Han et al., 2014).

$$\text{glucose} + \text{AuOH} \rightarrow \text{gluconolactone} + \text{Au} \quad (1)$$

In alkaline solutions Au forms AuOH due to the reaction between OH^- ions in the basic electrolyte and the Au^+ ions on the surface structure (Coyle et al., 2017). A reversible transition between Co_3O_4 and CoOOH occurs on the surface in the presence of glucose which is represented by Eqn. (2) (Ding et al., 2010). Due to the shift in potential to the negative, a secondary reaction took place converting CoOOH to CoO_2 on the surface which is expressed by Eqn. (3) (Ramasamy et al., 2015) with the overall mechanism described in Eqn. (4) (Ding et al., 2010).

$$Co_3O_4 + OH^- + H_2O \rightarrow 3CoOOH + e^- \quad (2)$$

$$CoOOH + OH^- \rightarrow CoO_2 + H_2O + e^- \quad (3)$$

$$2CoO_2 + \text{glucose} \rightarrow 2CoOOH + \text{gluconolactone} \quad (4)$$

Similarly Co_3O_4 structures have been studied in the presence of glucose however due to the lack of Au in the structure, the glucose oxidation peak occurs at a much higher on-set potential (~0.5) (Ding et al., 2010; Kung et al., 2011) effecting the selectivity of the sensor. This desired mechanism is best observed through an alkaline electrolyte such as the KOH used in these studies, where a concentration of 0.5 M was chosen in this study as blood is slightly alkaline. As the CV peak at +0.1 V shows a high electrocatalytic activity towards glucose, chronoamperometry was performed at this onset potential to analyse its sensing capabilities in the presence of glucose. Fig. 4B shows the additions analysis of the Au/Co_3O_4 sensor in the presence of 0.5 M KOH with a large range of glucose concentrations (20 µM and 10 mM). The chronoamperometric additions analysis is further evidenced by the multiple linear regression lines (Supplementary information S6) showing two distinct linear ranges for the Au/Co_3O_4 sensor. To detail the linear regions more specifically two linear regression regions were found for the sensor giving two separate sensitivities depending on the glucose concentration. Ranging between 20 µM and 100 µM (Supplementary information S6A) a very large, sharp peak was observed

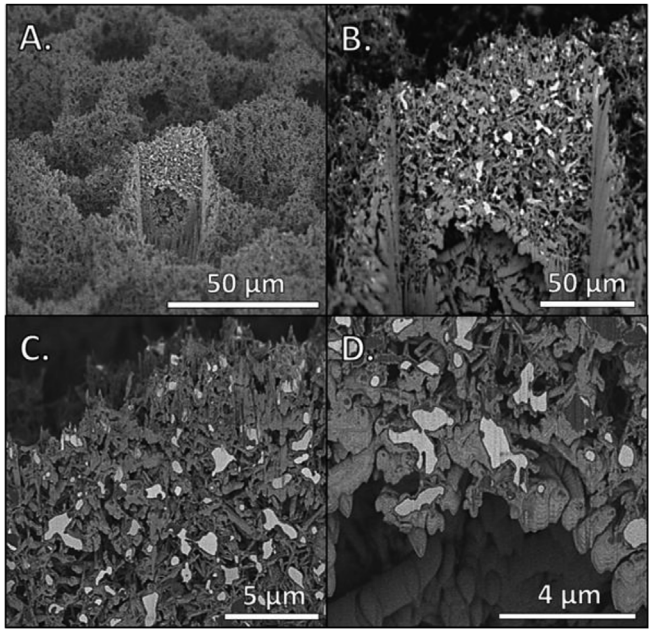

Fig. 2. (A) Low magnification side-imaging of the 100 mM sample after laser cutting followed by (B) higher magnification backscatter imaging; (C) High magnification backscatter imaging of the top and (D) bottom portions of the lattice.

equating to a calculated sensitivity of 2.014 mA mM^{-1}·cm^{-2}. A secondary linear region ranging between 2 mM and 10 mM (Supplementary information S6B) had a calculated sensitivity of 0.011 mA mM^{-1}·cm^{-2}, which corresponds to the blood glucose monitoring range of 3–8 mM. An experimental detection limit (Supplementary information S7) of 20 µM was observed from the initial addition of glucose to the 0.5 M KOH solution, showing the effectiveness of the sensing capabilities of the surface in the presence of very low glucose concentrations. This detection limit is much lower than common commercially available glucose sensors of recent times (~2.2 mM) (Lee et al., 2019). Comparatively Au honeycomb was also analysed with chronoamperometric additions analysis (Fig. 4C) showing a much lower electroactivity in the presence of glucose. A large increase in current response between the plain Au (0.146 mA cm^{-2}) and the Au/Co_3O_4 composite material (0.348 mA cm^{-2}) is observed by a factor of 2.39 showing the addition of Co_3O_4 to the surface of the Au more than doubled the glucose sensitivity. Uninterrupted chronoamperometric analysis was then performed for selectivity analysis in the presence of common physiological contaminants (Fig. 4D). The contaminants analysed were ascorbic acid, sucrose, fructose, maltose, lactose and uric acid. Little to no electrochemical signal was produced with each addition to the 0.5 M KOH solution showing the sensor is specifically catered to glucose concentrations. A subsequent glucose addition of 10 mM was introduced to the contaminants solutions showing a large current response. Due to the presence of Au in the material the on-set potential, where glucose electrooxidation is at its maximum, has been reduced to +0.1 V. Metal oxides tend to display a glucose peak with a much higher on-set potential, where common physiological contaminants display higher current responses with larger on-set potentials which can severely affect the sensors response capabilities towards glucose (Lang et al., 2013). This confirms excellent selectivity towards glucose with the further conclusion that the presence of common physiological sugars and acids do not affect the sensors performance. Repeatability analysis (Supplementary information S8) was then performed on the sensor with 5 consecutive cycles in the presence of 10 mM glucose with a slight reduction in output performance to 91%, thus showing excellent sensing performance over multiple cycles.

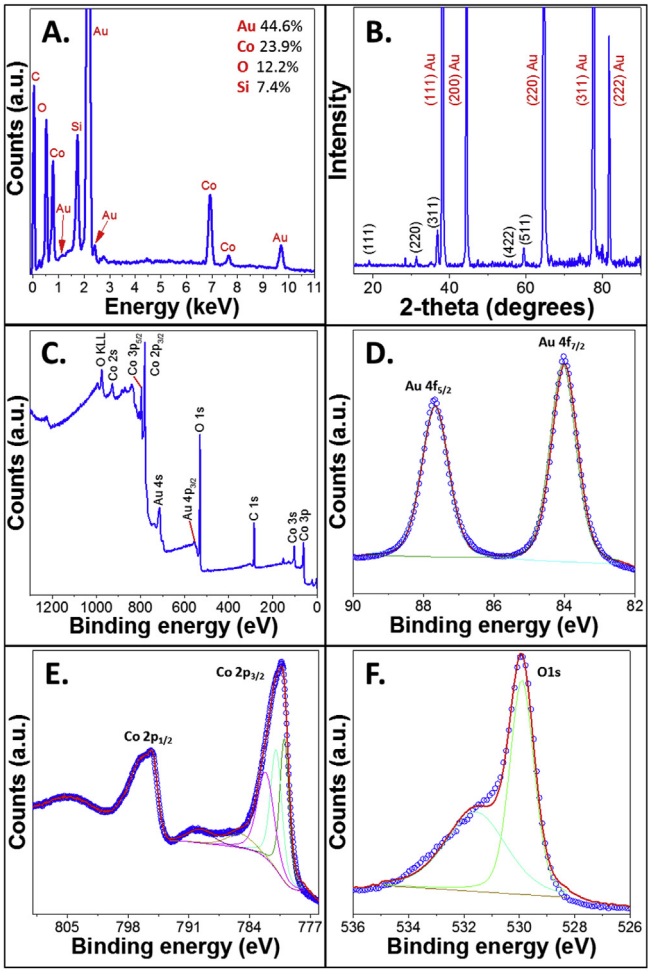

Fig. 3. Characterization of Au needles with 100 mM $CoCl_2$ (A) EDX spectral analysis, (B) XRD analysis (C) XPS survey spectra (D) XPS analysis of gold (E) XPS spectra of cobalt and (F) XPS spectra of oxygen. (For interpretation of the references to colour in this figure legend, the reader is referred to the Web version of this article).

3.3. Au honeycomb/Co_3O_4 needle sensing in synthetic saliva

Due to the low concentration range of glucose in saliva (0.03–0.08 mM) and the very high sensitivity of the developed sensor within this glucose concentration range (2.014 mA mM^{-1}·cm^{-2}), electroanalytical testing was extended to the detection of glucose in synthetic saliva. To explore this system, CV analysis was performed in the presence (80 µM) and absence of glucose (Fig. 5A) in synthetic saliva. A singular peak is formed through the oxidation of glucose ranging between +0.015 and + 0.25 V with a peak maximum at +0.15 V. Based on the similar peak position in Fig. 4A, the onset potential for chronoamperometric analysis was fixed at +0.1 V. The use of +0.1 V remains consistent with our previous studies for glucose detection in the human range for blood. The chronoamperometric additions analysis (Fig. 5B) was then performed in synthetic saliva with increasing concentrations of glucose ranging between 20 µM and 1 mM (similar to common glucose concentrations in saliva) (Ye et al., 2013). The calibration curve of the additions analysis (Supplementary information S9) showed an overall sensitivity of 0.0235 mA mM^{-1}·cm^{-2} with an R^2 value of 0.98. Increasing current responses with incremental additions showed a good sensitivity for the low concentration range. This sensitivity demonstrates the sensor's capability to detect glucose in the synthetic saliva, showing great promise for the non-invasive detection of physiological glucose levels. Long term stability of the sensor was

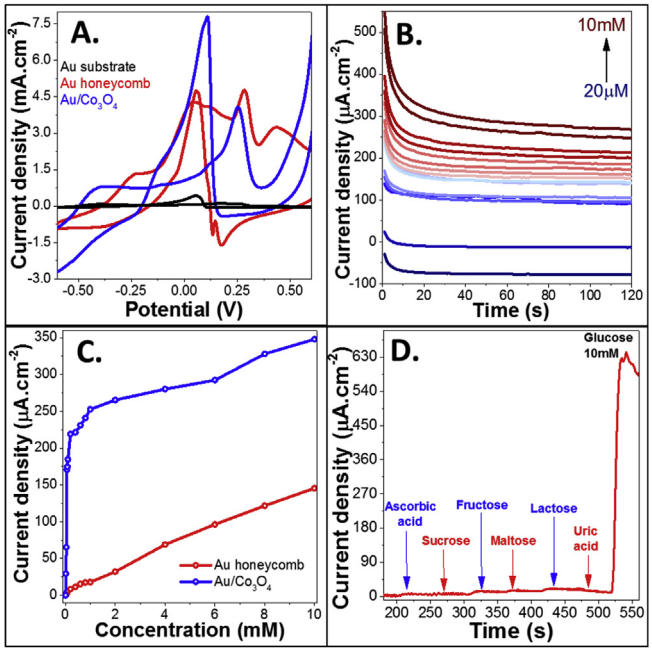

Fig. 4. (A) CV analysis of Au (black), Au honeycomb (red) and Au/Co_3O_4 (blue) in 0.5 M KOH and 10 mM glucose (B) chronoamperometric analysis of Au/Co_3O_4 with additions of glucose ranging between 20 μM and 10 mM (C) comparison graphs of chronoamperometric additions analysis for Au honeycomb (red) and Au/Co_3O_4 and (D) chronoamperometric additions analysis of Au/Co_3O_4 in the presence of common physiological contaminants. (For interpretation of the references to colour in this figure legend, the reader is referred to the Web version of this article).

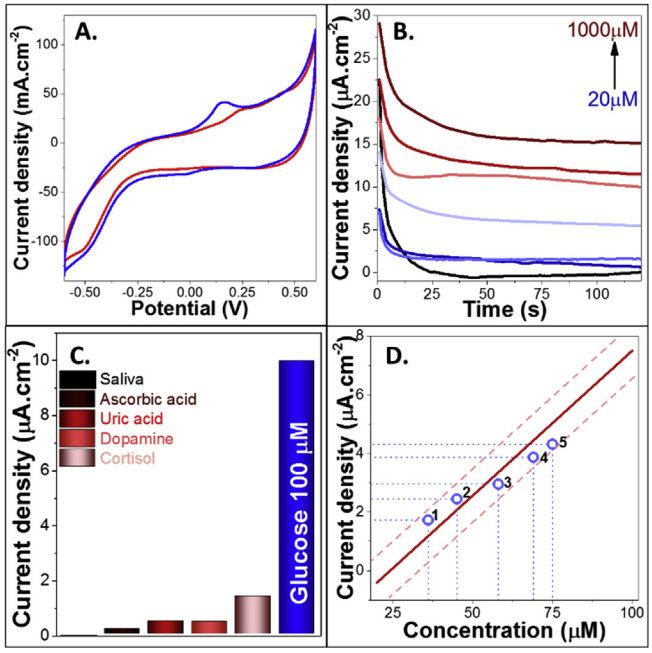

Fig. 5. (A) CV analysis of Au/Co_3O_4 in synthetic saliva with (blue) and without (red) 80 μM glucose. (B) Chronoamperometric analysis of Au/Co_3O_4 in the presence of synthetic saliva with 20 μM and 1 mM glucose. (C) Current density response for physiological contaminants in the presence of synthetic saliva and (D) Calibration curve (red) of current density vs concentration for glucose additions in the presence of synthetic saliva with 5 additions of unknown glucose concentrations (blue). (For interpretation of the references to colour in this figure legend, the reader is referred to the Web version of this article).

performed in synthetic saliva with glucose (Supplementary information S10) showing the current response of the sensor reducing slowly over time. The current response reduction is due to the saturation of the sensors surface due to glucose, therefore impeding the current response of the sensor over extended periods of time. Contaminants analysis was performed on the sensor (Supplementary information S11) with the additions of 2.4 μM ascorbic acid, 1.6 μM uric acid, 1.6 μM dopamine and 0.22 μM cortisol (Campos et al., 2018) followed by 100 μM glucose. Fig. 5C displays the current response in the form of a bar graph for each addition after a stability time of 120 s was reached. From these additions ascorbic acid showed a very small response magnitude of 0.185 μA cm^{-2} (1.3% of glucose response), with uric acid showing 0.471 μA cm^{-2} (3.3% vs glucose response). Dopamine showed a miniscule decrease in current response to 0.455 μA cm^{-2} (3.2% of glucose response) while cortisol showed the largest effect to the current response, increasing to 1.384 μA cm^{-2} (9.7% of glucose response). Overall the effect of each contaminant was in the acceptable range (± 10%) as the current response after the addition of 100 μM glucose was 9.98 μA cm^{-2}, within a similar range to our previous glucose response analysis. The results indicate that the sensor is not only selective in KOH medium but also in synthetic saliva thus making it feasible to be used for non-invasive diagnostic applications. To test the real-life application and repeatability of the sensor, 5 unknown solutions of glucose (within the concentration range of 20–80 μM) were tested. Initially a calibration curve was formed using the 120 s response current for each glucose addition from the additions analysis (Supplementary information S9). Using this calibration curve and the current response for the unknown additions, data points were added to the graph and analysed for their percentage change compared to the calibration line (Fig. 5D). In analysing the change in concentration between the 'unknown' solution and the calibration curve concentration (Supporting information Table S3), an average percentage change of 9.7% with the variance of results ranging between a percentage range of 7.8 and 13.3%. The unknown solutions analysis and excellent selectivity in the presence of common physiological contaminants in both blood and saliva shows very promising capabilities for glucose biosensor which can be used for non-invasive diagnosis applications.

4. Conclusions

In this study we have presented an easily synthesised porous Au structure with Co_3O_4 needles cohesively and seamless coating the Au surface whilst retaining its porosity and macro-structure. XRD and XPS analysis showed the clear representation of Au and Co_3O_4 on the surface, with the combination of the two components observed in cyclic voltammetry analysis in the presence of glucose. Excellent electrochemical sensing performance of the structure was observed in the present of glucose with a calculated sensitivity of 2.014 mA $mM^{-1}{\cdot}cm^{-2}$ within the range of 0–0.1 mM and 0.011 mA $mM^{-1}{\cdot}cm^{-2}$ within 2–10 mM glucose. A very low experimental detection limit of 20 μM makes this sensor very attractive for applications involving saliva, sweat and tear based electrochemical glucose sensors. Little or no cross-interference was observed in the presence of common physiological contaminants such as AA and UA and common biological sugars. Further to this, glucose detection in synthetic saliva showed excellent calculated sensitivity of 0.0235 mA $mM^{-1}{\cdot}cm^{-2}$ with minimal effect by interfering species commonly found in saliva such as cortisol and dopamine. These results showed that the fabricated sensor is highly capable for non-invasive diagnostic applications.

Declaration of interests

The authors declare that they have no known competing financial interests or personal relationships that could have appeared to influence the work reported in this paper.

CRediT authorship contribution statement

Victoria E. Coyle: Conceptualization, Investigation, Visualization, Formal analysis, Writing - original draft, Writing - review & editing. **Ahmad E. Kandjani:** Conceptualization, Investigation, Visualization, Formal analysis, Writing - review & editing. **Matthew R. Field:** Formal analysis, Writing - review & editing. **Patrick Hartley:** Investigation, Funding acquisition, Writing - review & editing. **Miao Chen:** Investigation, Funding acquisition, Writing - review & editing. **Ylias M. Sabri:** Supervision, Conceptualization, Investigation, Formal analysis, Writing - original draft, Writing - review & editing. **Suresh K. Bhargava:** Supervision, Project administration, Funding acquisition, Investigation, Formal analysis, Writing - review & editing.

Acknowledgements

The authors acknowledge the RMIT Microscopy and Microanalysis Facility (RMMF) for allowing the use of their comprehensive facilities and services. The authors thank Mr Ciao Yuxun for his technical support. The authors thank CSIRO Mineral Resources for the PhD scholarship support. A.E.K. thanks RMIT University for a Vice Chancellor's Postdoctoral Fellowship.

Appendix A. Supplementary data

Supplementary data to this article can be found online at https://doi.org/10.1016/j.bios.2019.111479.

References

Anderson, K., Poulter, B., Dudgeon, J., Li, S.-E., Ma, X., 2017. Sensors 17 (8), 1807.
Aoun, S.B., Dursun, Z., Koga, T., Bang, G.S., Sotomura, T., Taniguchi, I., 2004. J. Electroanal. Chem. 567 (2), 175–183.
Association, A.D., 2018. Diabetes Care 41 (5), 917.
Bandodkar, A.J., Wang, J., 2014. Trends Biotechnol. 32 (7), 363–371.
Barry, E., Roberts, S., Oke, J., Vijayaraghavan, S., Normansell, R., Greenhalgh, T., 2017. BMJ 356, i6538.
Bertoncello, P., Ugo, P., 2003. J. Braz. Chem. Soc. 14 (4), 517–522.
Biesinger, M.C., Payne, B.P., Grosvenor, A.P., Lau, L.W.M., Gerson, A.R., Smart, R.S.C., 2011. Appl. Surf. Sci. 257 (7), 2717–2730.
Boisselier, E., Astruc, D., 2009. Chem. Soc. Rev. 38 (6), 1759–1782.
Campos, A.M., Raymundo-Pereira, P.A., Mendonça, C.D., Calegaro, M.L., Machado, S.A., Oliveira Jr., O.N., 2018. ACS Appl. Nano Mater. 1 (2), 654–661.
Casaletto, M., Longo, A., Martorana, A., Prestianni, A., Venezia, A., 2006. Surf. Interface Anal. 38 (4), 215–218.
Chaisiwamongkhol, K., Batchelor-McAuley, C., Compton, R.G., 2017. Analyst 142 (15), 2828–2835.
Chakraborty, P., Dhar, S., Debnath, K., Majumder, T., Mondal, S.P., 2019. Sensor. Actuator. B Chem. 283, 776–785.
Chen, L., Fujita, T., Ding, Y., Chen, M., 2010. Adv. Funct. Mater. 20 (14), 2279–2285.
Cheng, T.-M., Huang, T.-K., Lin, H.-K., Tung, S.-P., Chen, Y.-L., Lee, C.-Y., Chiu, H.-T., 2010. ACS Appl. Mater. Interfaces 2 (10), 2773–2780.
Coyle, V.E., Kandjani, A.E., Sabri, Y.M., Bhargava, S.K., 2017. Electroanalysis 29 (1), 294–304.
Coyle, V.E., Oppedisano, D.K., Jones, L.A., Kandjani, A.E., Sabri, Y.M., Bhargava, S.K., 2016. J. Electrochem. Soc. 163 (14), B689–B695.
Daima, H.K., Selvakannan, P., Shukla, R., Bhargava, S.K., Bansal, V., 2013. PLoS One 8 (10), e79676.
Ding, Y., Liu, Y., Parisi, J., Zhang, L., Lei, Y., 2011. Biosens. Bioelectron. 28 (1), 393–398.
Ding, Y., Wang, Y., Su, L., Bellagamba, M., Zhang, H., Lei, Y., 2010. Biosens. Bioelectron. 26 (2), 542–548.
Dong, X.-C., Xu, H., Wang, X.-W., Huang, Y.-X., Chan-Park, M.B., Zhang, H., Wang, L.-H., Huang, W., Chen, P., 2012. ACS Nano 6 (4), 3206–3213.
Han, L., Zhang, S., Han, L., Yang, D.-P., Hou, C., Liu, A., 2014. Electrochim. Acta 138, 109–114.
Ibupoto, Z.H., Elhag, S., AlSalhi, M., Nur, O., Willander, M., 2014. Electroanalysis 26 (8), 1773–1781.
Kabir, K.M., Sabri, Y.M., Kandjani, A.E., Matthews, G.I., Field, M., Jones, L.A., Nafady, A., Ippolito, S.J., Bhargava, S.K., 2015. Langmuir 31 (30), 8519–8529.
Kimmel, D.W., LeBlanc, G., Meschievitz, M.E., Cliffel, D.E., 2011. Anal. Chem. 84 (2), 685–707.
Kownacka, A.E., Vegelyte, D., Joosse, M., Anton, N., Toebes, B.J., Lauko, J., Buzzacchera, I., Lipinska, K., Wilson, D.A., Geelhoed-Duijvestijn, N., 2018. Biomacromolecules 19 (11), 4504–4511.
Kung, C.-W., Lin, C.-Y., Lai, Y.-H., Vittal, R., Ho, K.-C., 2011. Biosens. Bioelectron. 27 (1), 125–131.
Lang, X.-Y., Fu, H.-Y., Hou, C., Han, G.-F., Yang, P., Liu, Y.-B., Jiang, Q., 2013. Nat. Commun. 4, 2169.
Lankelma, J., Nie, Z., Carrilho, E., Whitesides, G.M., 2012. Anal. Chem. 84 (9), 4147–4152.
Lay, B., Coyle, V.E., Kandjani, A.E., Amin, M.H., Sabri, Y.M., Bhargava, S.K., 2017. J. Mater. Chem. B 5 (5), 5441–5449.
Lee, I., Loew, N., Tsugawa, W., Ikebukuro, K., Sode, K., 2019. Biosens. Bioelectron. 124–125, 216–223.
Liu, X., Chang, Z., Luo, L., Xu, T., Lei, X., Liu, J., Sun, X., 2014. Chem. Mater. 26 (5), 1889–1895.
Mei, W., Huang, J., Zhu, L., Ye, Z., Mai, Y., Tu, J., 2012. J. Mater. Chem. 22 (18), 9315–9321.
Moyer, J., Wilson, D., Finkelshtein, I., Wong, B., Potts, R., 2012. Diabetes Technol. Ther. 14 (5), 398–402.
Nohira, H., Tsai, W., Besling, W., Young, E., Petry, J., Conard, T., Vandervorst, W., De Gendt, S., Heyns, M., Maes, J., Tuominen, M., 2002. J. Non-Cryst. Solids 303 (1), 83–87.
Pearson, A., O'Mullane, A.P., Bansal, V., Bhargava, S.K., 2011. Inorg. Chem. 50 (5), 1705–1712.
Plowman, B.J., O'Mullane, A.P., Bhargava, S.K., 2011. Faraday Discuss 152, 43–62.
Plowman, B.J., O'Mullane, A.P., Selvakannan, P., Bhargava, S.K., 2010. Chem. Commun. 46 (48), 9182–9184.
Ramasamy, R., Ramachandran, K., Philip, G.G., Ramachandran, R., Therese, H.A., Gnana kumar, G., 2015. RSC Adv. 5 (93), 76538–76547.
Raymundo-Pereira, P.A., Shimizu, F.M., Coelho, D., Piazzeta, M.H., Gobbi, A.L., Machado, S.A., Oliveira Jr., O.N., 2016. Biosens. Bioelectron. 86, 369–376.
Roberts, K., Jaffe, A., Verge, C., Thomas, P.S., 2012. J. Diabetes Sci. Technol. 6 (3), 659–664.
Solanki, P.R., Kaushik, A., Agrawal, V.V., Malhotra, B.D., 2011. NPG Asia Mater. 3 (1), 17.
Teixeira, M.F., Bergamini, M.F., Marques, C.M., Bocchi, N., 2004a. Talanta 63 (4), 1083–1088.
Teixeira, M.F., Marcolino-Júnior, L.H., Fatibello-Filho, O., Dockal, E.R., Cavalheiro, É.T., 2004b. J. Braz. Chem. Soc. 15 (6), 803–808.
Toghill, K.E., Compton, R.G., 2010. Int. J. Electrochem. Sci. 5 (9), 1246–1301.
Tong, G.-X., Liu, F.-T., Wu, W.-H., Shen, J.-P., Hu, X., Liang, Y., 2012. CrystEngComm 14 (18), 5963–5973.
Wang, G., He, X., Wang, L., Gu, A., Huang, Y., Fang, B., Geng, B., Zhang, X., 2013. Microchim. Acta 180 (3–4), 161–186.
Wang, J., 2008. Chem. Rev. 108 (2), 814–825.
Wang, W., Li, Z., Liu, L., Zhang, H., Zheng, W., Wang, Y., Huang, H., Wang, Z., Wang, C., 2009. Sensor. Actuator. B Chem. 141 (2), 404–409.
Yang, J., Liu, H., Martens, W.N., Frost, R.L., 2010. J. Phys. Chem. C 114 (1), 111–119.
Yao, H., Shum, A.J., Cowan, M., Lähdesmäki, I., Parviz, B.A., 2011. Biosens. Bioelectron. 26 (7), 3290–3296.
Ye, D., Liang, G., Li, H., Luo, J., Zhang, S., Chen, H., Kong, J., 2013. Talanta 116, 223–230.
Zhang, Y., Chang, G., Liu, S., Lu, W., Tian, J., Sun, X., 2011. Biosens. Bioelectron. 28 (1), 344–348.
Zhu, H., Li, L., Zhou, W., Shao, Z., Chen, X., 2016. J. Mater. Chem. B 4 (46), 7333–7349.